CANCER

The role of Piezo1 mechanotransduction in high-grade serous ovarian cancer: Insights from an in vitro model of collective detachment

Hannah M. Micek[1], Ning Yang[2]†, Mayuri Dutta[1]†, Lauren Rosenstock[1], Yicheng Ma[1], Caitlin Hielsberg[1], Molly McCord[3,4], Jacob Notbohm[1,3,4,5], Stephanie McGregor[2,5], Pamela K. Kreeger[1,2,5]*

Slowing peritoneal spread in high-grade serous ovarian cancer (HGSOC) would improve patient prognosis and quality of life. HGSOC spreads when single cells and spheroids detach, float through the peritoneal fluid and take over new sites, with spheroids thought to be more aggressive than single cells. Using our in vitro model of spheroid collective detachment, we determine that increased substrate stiffness led to the detachment of more spheroids. We identified a mechanism where Piezo1 activity increased MMP-1/MMP-10, decreased collagen I and fibronectin, and increased spheroid detachment. Piezo1 expression was confirmed in omental masses from patients with stage III/IV HGSOC. Using OV90 and CRISPR-modified $PIEZO1^{-/-}$ OV90 in a mouse xenograft model, we determined that while both genotypes efficiently took over the omentum, loss of Piezo1 significantly decreased ascitic volume, tumor spheroids in the ascites, and the number of macroscopic tumors in the mesentery. These results support that slowing collective detachment may benefit patients and identify Piezo1 as a potential therapeutic target.

INTRODUCTION

High-grade serous ovarian cancer (HGSOC) has an overall 5-year survival rate of less than 50%, due to most patients having substantial metastatic burden at the time of diagnosis. While early-stage tumors are restricted to the fallopian tube and ovary, at advanced stages, tumors are present through the pelvis and peritoneal cavity (*1*). Patients diagnosed at stage III/IV frequently have metastases on deposits of visceral adipose (e.g., omentum and small bowel mesentery) and accumulation of excess fluid, termed ascites. Identifying methods to slow or stop spread and ascites accumulation would improve patient prognosis and quality of life, as metastases can ultimately constrict the bladder or bowel and ascites causes substantial discomfort. However, HGSOC metastasis differs from that of most solid tumors. Rather than relying on hematogenous or lymphatic spread, tumor cells detach, float in the peritoneal fluid/ascites, and reattach to establish new tumors (*2*). The processes regulating transport and reattachment have been studied through in vitro (*3–6*) and in vivo models (*7, 8*), but analysis of the detachment process is much more challenging.

Tumor cells that have detached can be isolated from ascites as both single cells and spheroids of cells on the order of 50 to 100 μm in diameter (*9, 10*). While most studies of HGSOC metastasis have used single cells, spheroids are believed to disproportionately contribute to metastasis due to their resistance to apoptosis and chemotherapy (*11*). To examine how spheroids are generated, Al Habyan *et al.* (*12*) used labeled tumor cells injected into the ovary to demonstrate that many spheroids arose from the same ovary. These data suggest that tumor cells either aggregate quickly after detaching or are released as a unit through a process of collective detachment. Unfortunately, animal models are not easily adapted to address what controls the extent of detachment and whether a tumor cell releases as a single cell or in a spheroid. Therefore, we recently developed an in vitro model that isolates tumor cells that detach as spheroids from cells that detach as single cells (*9*). In this model, ovarian cancer cells are cultured on top of a polyacrylamide (PAA) gel that rests within a cell strainer (Fig. 1A). As individual cells detach, they pass through the strainer, while spheroids that have collectively detached (Sph-CD) are trapped by the filter and can be isolated for further analysis.

Here, we sought to use our model to begin testing the hypothesis that changes in the tumor microenvironment associated with disease progression increase collective detachment. When designing biomimetic systems, determining how to best mimic the extracellular matrix (ECM) is an essential first step before building in higher-order interactions (*13*). The role of the ECM in HGSOC has been examined in many of the existing culture systems to understand tumor cell adhesion, spreading, and proliferation [reviewed in (*2*)], but it is unknown whether it affects cell detachment. While there are many changes in the ECM as HGSOC progresses, the most abundant ECM protein is collagen I (Col I), which increases 20-fold by advanced stages (*14*). Associated with this increase in ECM is an increase in stiffness. This fibrotic response is observed in numerous solid tumors, including breast cancer, which is known to use collective processes in metastasis (*15*). Using PAA gel formulations with stiffnesses reflective of healthy and metastatic omentum along with different concentrations of Col I, we were able to test the individual and combinatorial effects of increased Col I density and substrate stiffness. We then examined downstream signaling processes to identify mechanisms regulating collective detachment and analyzed the effect of slowing collective detachment on tumor progression in vivo.

[1]Department of Biomedical Engineering, University of Wisconsin-Madison, Madison, WI 53705, USA. [2]Department of Pathology and Laboratory Medicine, University of Wisconsin School of Medicine and Public Health, Madison, WI 53705, USA. [3]Department of Mechanical Engineering, University of Wisconsin-Madison, Madison, WI 53705, USA. [4]Biophysics Program, University of Wisconsin-Madison, Madison, WI 53705, USA. [5]University of Wisconsin Carbone Cancer Center, University of Wisconsin School of Medicine and Public Health, Madison, WI 53705, USA.
*Corresponding author. Email: kreeger@wisc.edu
†These authors contributed equally to this work.
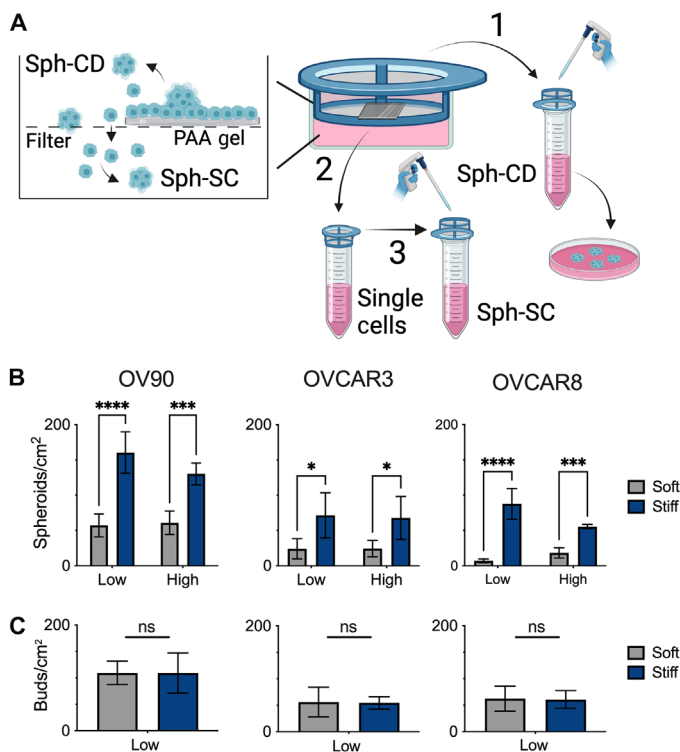
Fig. 1. Stiffness increases collective detachment of spheroids. (**A**) Overview of culture system consisting of a PAA gel on top of a filter. At the completion of culture, the cover slip and PAA gel were removed for analysis. To isolate the Sph-CD (#1), the filter was inverted and captured spheroids were washed out. To isolate single cells (#2), the media was collected from the bottom well and passed through a cell strainer. Last, to isolate Sph-SC (#3), the cell strainer used to isolate single cells was inverted and washed to remove captured spheroids. All three fractions were then transferred to cell culture dishes to image and quantify. (**B**) Quantification of OV90, OVCAR3, and OVCAR8 Sph-CD from soft (5 kPa) or stiff (44 kPa) PAA gels functionalized with a low (100 μg/ml) or high (2000 μg/ml) Col I. (**C**) Quantification of OV90, OVCAR3, and OVCAR8 buds on soft or stiff PAA gels functionalized with Col I (100 μg/ml), five fields of view were averaged per gel. Data in (B) and (C) are the average ± SD of $N = 3$ to 4 individual gels. Statistical tests are two-way analysis of variance (ANOVA) with Tukey's (B) and unpaired t test (C). ns indicates not statistically significant. *$P < 0.05$, ***$P < 0.001$, and ****$P < 0.0001$.

RESULTS

Increased substrate stiffness leads to increased collective detachment of ovarian cancer cells

We first sought to determine the approximate stiffness of the omentum of a healthy female and a female with stage III/IV HGSOC. It is particularly challenging to collect and process these tissue samples through pathology while maintaining physiological temperatures to prevent changes in lipid structure and the resulting mechanics. In the literature, the moduli of these tissues at high strains (15 to 30%) range from 3 to 32 kPa (healthy) and 15 to 100 kPa (disease) (*14*, *16*, *17*). This uncertainty results from differences in sample collection (with some studies using tissue subjected to a freeze/thaw cycle) and mechanical testing procedures. As an alternative approach to define our range, we first generated a series of PAA gels of varying stiffness (Young's modulus from 2 to 44 kPa, determined from stress-strain curve by dynamic mechanical analyzer) and then asked a blinded gynecologic oncologist to palpate the gels as they would do to tissue

during a debulking surgery. On the basis of their assessment, PAA at ~5 kPa was representative of benign tissue ("soft"), and ~44 kPa was representative of metastatic tissue ("stiff"; fig. S1A). We then modified soft and stiff PAA gels with either low (100 μg/ml) or high (2000 μg/ml) Col I (fig. S1B). Last, we considered the cell types to incorporate into our model. Our prior analysis of spheroids isolated from patient ascites suggested that they are composed primarily of epithelial cells (*9*). However, it is possible that the originating site has more cellular diversity. Therefore, we immunostained tumors from patients with stage III/IV HGSOC for Pax8 (tumor cells), CD68 (monocytes/macrophages), and αSMA (activated fibroblasts). Large areas of the tumor were composed of only Pax8^{+} cells, with monocytes/macrophages and fibroblasts between these regions [fig. S1C; similar findings were observed with respect to fibroblasts in our prior work (*18*)]. On the basis of these findings, we used only tumor cells in our model to examine the impact of stiffness and ECM density.

Using the selected stiffnesses and ECM densities, we observed a significant increase in Sph-CD with culture on stiff substrates across three different cell lines, but no significant differences observed with respect to Col I density (Fig. 1B). While these observations were based on counting a sampling of the released aggregates, quantification of total DNA from released OV90 Sph-CD also showed that stiffness, but not ECM density, increased collective detachment (fig. S1D). To confirm that the increase in Sph-CD was not due to an increase in all forms of cell detachment, we quantified single cells and spheroids resulting from single cells that aggregated (Sph-SC) and found that there were no significant differences with respect to substrate stiffness or ECM density (fig. S1E). Before spheroid detachment, we observed areas of high cell density and cellular mounding on the surface of the substrate (fig. S1F). These areas were termed buds and appear to be the sites where Sph-CD detach. As more bud formation would explain the increase in Sph-CD, we quantified buds across the substrates and determined there were no significant differences (Fig. 1C; note that in remaining figures, only data for OV90 are shown with data from the other lines in supplement). However, we note that the average bud size is larger than the average aggregate size (fig. S1G), suggesting that only a portion of the bud detaches.

Increased collective detachment was not a result of well-established effects of stiffness

While the number of buds was similar across conditions and buds were similar in size on soft and stiff substrates, it is possible that more actively proliferating buds would be less stable and therefore more likely to detach. As prior studies have clearly established a link between increased stiffness and cell proliferation in some contexts (*19*, *20*), we examined whether proliferation was involved in collective detachment. We first observed that inhibition of proliferation with aphidicolin ablated the stiffness-dependent increase in Sph-CD (Fig. 2A and fig. S2, A and B). However, there was no difference in overall proliferation between soft and stiff substrates (fig. S2C) or for proliferation localized to buds or the monolayer (Fig. 2, B and C). To better understand the role of proliferation in collective detachment, we examined the monolayer from cells treated with vehicle or aphidicolin and observed a significant decrease in the number of buds on both stiffnesses (fig. S2D), suggesting that proliferation is needed to generate many buds. As the number of buds and proliferation were not affected by stiffness, we hypothesized that stiffness may instead affect detachment.
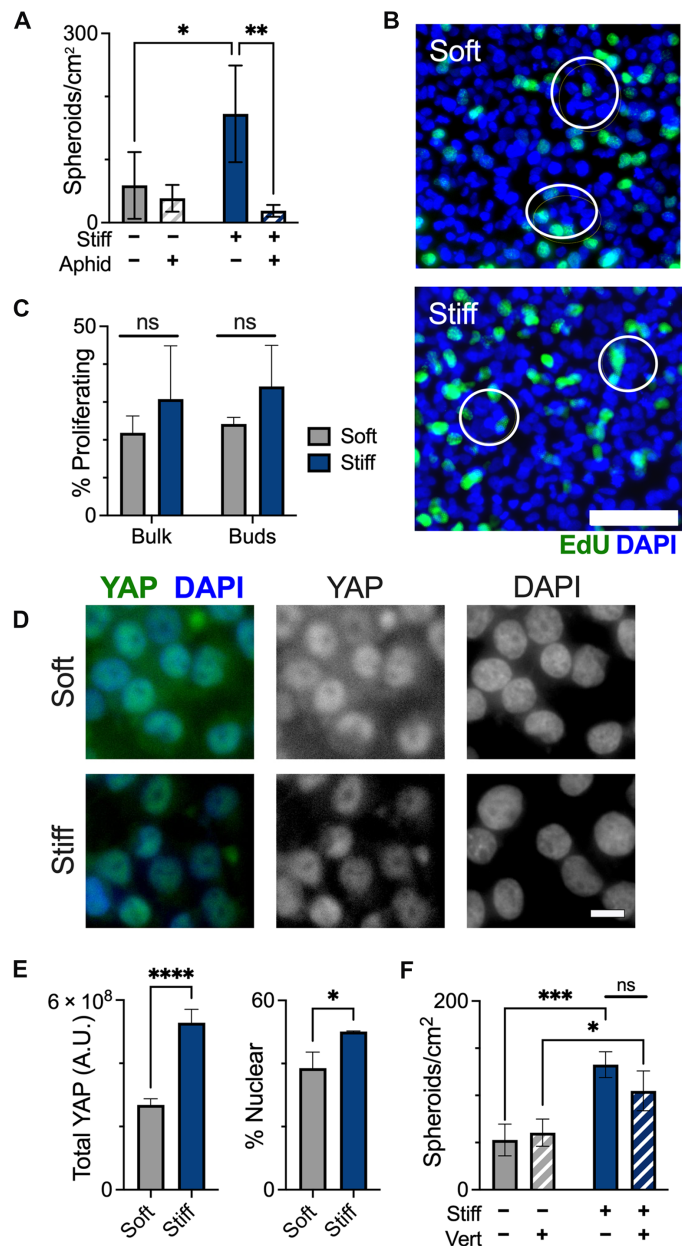
Fig. 2. Stiffness-induced proliferation and YAP signaling are not responsible for increased collective detachment. (**A**) Quantification of OV90 Sph-CD from soft or stiff gels treated with vehicle [dimethyl sulfoxide (DMSO)] or aphidicolin (4 μg/ml) to inhibit proliferation. (**B**) Representative images from Click-iT EdU staining of OV90 cells seeded on soft or stiff PAA gels. Spheroid buds are circled in white. (**C**) Quantification of proliferating OV90 cells within buds on the gel or in the monolayer (bulk) for soft and stiff gels, three fields of view were averaged per gel. (**D**) Representative images of YAP immunostaining (green) for OV90 on soft and stiff gels. (**E**) Total YAP signal and percentage of YAP localized to the nucleus quantified from immunofluorescent images of OV90 cells seeded on soft or stiff substrates, three fields of view were averaged per gel. (**F**) Quantification of OV90 Sph-CD from soft or stiff PAA gels treated with vehicle (DMSO) or 2 μM verteporfin to inhibit YAP. For (A), (C), (E), and (F), data shown are the average ± SD of $N = 3$ to 6 individual gels per condition. Statistical tests are two-way ANOVA with Tukey's [(A), (C), and (F)], unpaired t test (E). *$P < 0.05$, **$P < 0.01$, ***$P < 0.001$, ****$P < 0.0001$. Scale bars, 100 μm (B) and 10 μm (D). DAPI, 4′,6-diamidino-2-phenylindole; A.U., arbitrary units.

We next investigated the potential role of mechanosensitive transcription factor YAP in stiffness-induced collective detachment. YAP is a transcription factor in the Hippo pathway activated in response to increased stiffness (*21*) and linked to tumor cell migration and invasion (*22*). Immunostaining confirmed that the ovarian cancer lines expressed YAP and that increased stiffness led to increased expression and nuclear localization (Fig. 2, D and E, and fig. S3A). To test whether YAP signaling in response to stiffness affects collective detachment, cultures were treated with the inhibitor verteporfin (*23*). We observed an increase in Sph-CD in response to stiffness with both vehicle and verteporfin (Fig. 2F and fig. S3B). Neither stiffness nor YAP inhibition affected single-cell detachment and aggregation (fig. S3B). Together, these data suggest that YAP was activated with stiffness in our model but was not directly involved in the signaling underlying stiffness-induced collective detachment.

Piezo1 activity increases collective detachment of ovarian cancer cells

Next, we examined the role of stretch-activated ion channel Piezo1 in stiffness-induced collective detachment. While Piezo1 has been characterized as a mechanosensor for shear stress in the vasculature (*24*) and stretch in alveoli (*25*), it has a key role in cell extrusion initiated by cell crowding in homeostatic epithelial cell layers (*26*). Therefore, we added a Piezo1 antagonist [GsMTx-4; (*27*)] into the in vitro model and measured levels of Sph-CD from soft and stiff substrates. GsMTx-4 treatment led to a loss of stiffness-induced collective detachment in OV90 cells (Fig. 3A). GsMTx-4 can affect both Piezo1 and TRP channels; therefore, to confirm this result, we used CRISPR (fig. S4A) to knock out *PIEZO1* in OV90, OVCAR3, and OVCAR8 (*28*). Loss of Piezo1 was confirmed through quantitative reverse transcription polymerase chain reaction (qRT-PCR) and immunofluorescent staining, and minimal changes in proliferation rate were observed (fig. S4, B to D). When the knockout cells were cultured on soft and stiff substrates in the in vitro model, the stiffness-dependent increase in Sph-CD was lost (Fig. 3B and fig. S5A). Next, we treated wild-type cells seeded on soft and stiff substrates with Yoda1, a small-molecule agonist of Piezo1 (*29*). We observed a significant increase in Sph-CD from soft substrates with Yoda1 treatment, suggesting that Piezo1 activity is sufficient to facilitate spheroid collective detachment in the absence of other stiffness-dependent effects (Fig. 3C and fig. S5B). Despite the reported role of Piezo1 in cell extrusion from monolayers, we did not observe a change in single cells or Sph-SC in response to either *PIEZO1* KO or Yoda1 (fig. S5, A and B).

We next explored whether the dependence on Piezo1 resulted from changes in expression or activity on stiff substrates. *PIEZO1* expression in cells in the monolayer showed no difference between soft and stiff substrates (Fig. 3D). Likewise, immunostaining of the monolayer demonstrated similar levels of Piezo1 at the protein level (Fig. 3, E and F). This suggests that increased stiffness increases the activity of Piezo1, a force-dependent ion channel that is responsive to changes in membrane tension (*30*). While typically associated with activation by an external force such as shear, myosin-II–mediated tractions can lead to Piezo1 activity (*31*). As substrate stiffness can affect tractions, we used traction force microscopy and determined that tractions were significantly higher in cells on the stiffer substrates (Fig. 3G). When OV90 were treated with ML-7 to inhibit myosin light chain kinase, the number of Sph-CD was significantly decreased, consistent with a role for contractility (Fig. 3H). The number of buds was not affected by ML-7 treatment (fig. S5C), further
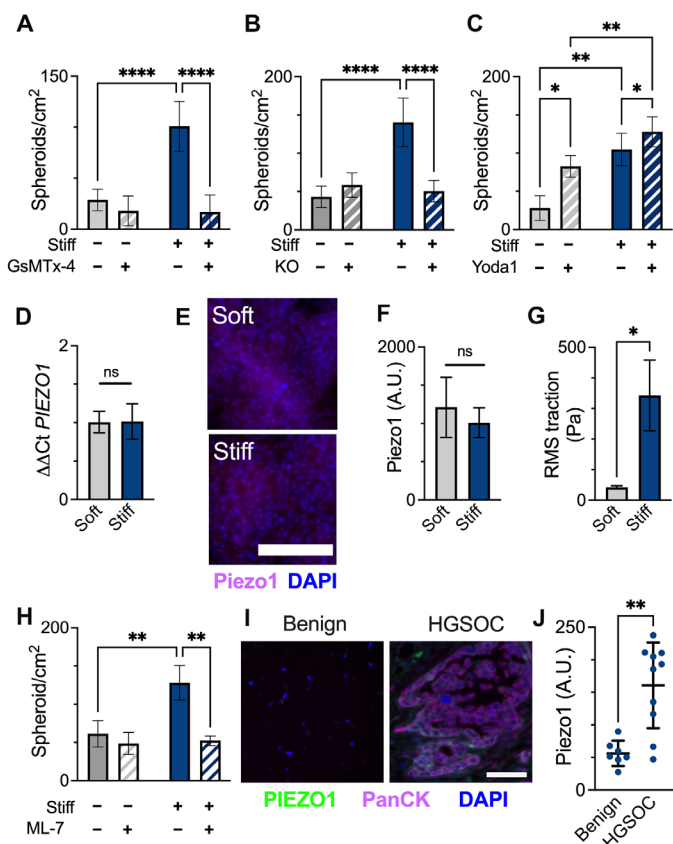
Fig. 3. Piezo1 activity is needed for stiffness-induced collective detachment. (**A**) Quantification of Sph-CD from OV90 cells on soft or stiff gels treated with vehicle (DMSO) or 10 μM GsMTx-4 to inhibit Piezo1. (**B**) Quantification of Sph-CD from wild-type (WT) OV90 or OV90 with *PIEZO1* knocked out (KO) by CRISPR on soft or stiff gels. (**C**) Quantification of Sph-CD from OV90 cells on soft or stiff gels treated with vehicle (DMSO) or 10 μM Yoda1 to activate Piezo1. (**D**) qRT-PCR for *PIEZO1* for OV90 cells on soft and stiff gels at 72 hours. Data are average ΔΔCt ± SD relative to *GAPDH* and soft gels, technical replicates. (**E**) Representative Piezo1 staining of OV90 on soft and stiff gels. (**F**) Piezo1 signal from OV90 cells seeded on soft or stiff gels, at least five fields of view were averaged per gel. (**G**) Root mean square (RMS) traction of OV-90 cells on soft and stiff substrates at 24 hours, two to five fields of view were averaged per gel. (**H**) Quantification of Sph-CD from OV90 cells seeded on soft or stiff gels treated with vehicle (DMSO) or 0.5 μM ML-7 to inhibit myosin light chain kinase. (**I**) Representative images of immunofluorescent staining of benign and HGSOC omenta for Piezo1. Pan-cytokeratin (PanCK) was used to mark tumor cells. (**J**) Integrated intensity of Piezo1 staining within the tissue, three fields of view were averaged per patient. For (A) to (H), data shown are the average ± SD of $N = 3$ to 5 individual gels per condition. In (J), data shown are the average ± SD of $N = 7$ to 10 patients per group. Statistical tests are two-way ANOVA with Tukey's [(A) to (C) and (H)], unpaired *t* test [(D) and (F)], unpaired *t* test with Welch's correction (G), Mann-Whitney test (J). *$P < 0.05$, **$P < 0.01$, and ****$P < 0.0001$. Scale bars, 100 μm.

supporting that proliferation-induced bud formation is independent of stiffness.

To confirm that Piezo1 has potential clinical relevance in HGSOC metastasis, we stained omenta from patients with stage III/IV HGSOC compared to patients without omental malignancies. As expected, malignancies in the omentum were associated with a stark increase in cellularity and Pan-CK^{+} tumor cells (Fig. 3I). Piezo1 was expressed both in the tumor bulk (defined as areas with consistent Pan-CK

expression) and in the stroma in stage III/IV HGSOC, while there was minimal Piezo1 detected in the absence of tumors (Fig. 3J).

Piezo1 activity increases MMP levels, resulting in remodeled ECM and increased collective detachment

The data indicate that the increase in Sph-CD is a result of Piezo1 activity specifically regulating spheroid release, as bud formation and proliferation were not affected by stiffness (Figs. 1C and 2, B and C) and Sph-CD were smaller than buds (fig. S1G). Spheroid release requires a loss of cell-cell and cell-ECM interactions between the spheroid and the substrate/monolayer. As Piezo1 activity has been shown to induce expression of matrix metalloproteinases (MMPs) (*32*, *33*), we evaluated whether MMP activity affected stiffness-induced collective detachment. Batimastat, a pan-MMP inhibitor, was incorporated into the model and found to negate the stiffness-induced increase in collective detachment (Fig. 4A and fig. S6A). This effect was specific to collective detachment, as there were no significant effects on single-cell detachment. To identify the specific MMPs contributing to stiffness-induced collective detachment, media from cells cultured on soft or stiff substrates was assayed for a set of eight MMPs (Fig. 4B and fig. S6B). Of the MMPs included in the screen, MMP-1 and MMP-10 were the most consistently expressed. MMP-1 was significantly up-regulated on stiff substrates in OV90 cells; while the level of MMP-1 was not affected by stiffness in OVCAR3 or OVCAR8 cells, we noted that the concentration in those conditions was comparable to the elevated level of OV90 on stiff substrates. MMP-10 was also significantly elevated on stiff substrates in OV90 cells and was increased but not statistically significant in response to stiffness for OVCAR3 and OVCAR8. As there are no specific inhibitors for MMP-1 or MMP-10 to isolate which MMP is responsible for increased detachment, we examined our Piezo1 knockout cells cultured on stiff substrates to determine which MMP was consistent with the Piezo1 mechanism. For all three cell lines, we observed a significant decrease in MMP-1 with loss of Piezo1 (Fig. 4C and fig. S6B).

While the media levels of MMP-1 and MMP-10 were not entirely consistent with the prior results for collective detachment, it is important to consider that MMPs will act locally on the ECM and that these effects may be different when bulk concentrations are only modestly different. MMP-1 is a collagenase that degrades Col I, and MMP-10 is a stromelysin that acts on several ECM components, including fibronectin (*34*, *35*). To determine whether the MMPs were affecting ECM organization of the substrate/buds, the PAA gels were stained with collagen-binding adhesion protein 35 (CNA35) and an antifibronectin antibody. CNA35–enhanced green fluorescent protein (EGFP) is a fluorescently tagged collagen-binding protein that preferentially labels fibrillar collagen (*36*), resulting in minimal background staining of the Col I covalently cross-linked to the PAA gel (fig. S7A). Cells on stiff substrates showed a marked reduction in Col I signal, consistent with the observation of elevated MMP-1 (Fig. 4D and fig. S7B). Fibronectin was also decreased on stiff substrates but not as strongly. qRT-PCR confirmed that transcription of *COL1A1* and *FN1* was not affected by stiffness (fig. S7C), supporting that these differences result from MMP activity. Combined, these data support that MMP-1 is elevated by Piezo1 activity, resulting in remodeling of the ECM in the monolayer and increased collective detachment.

Loss of Piezo1 slows tumor metastasis in vivo
To evaluate the impact of Piezo1-induced collective detachment in vivo, we used a xenograft model widely used to study metastasis in
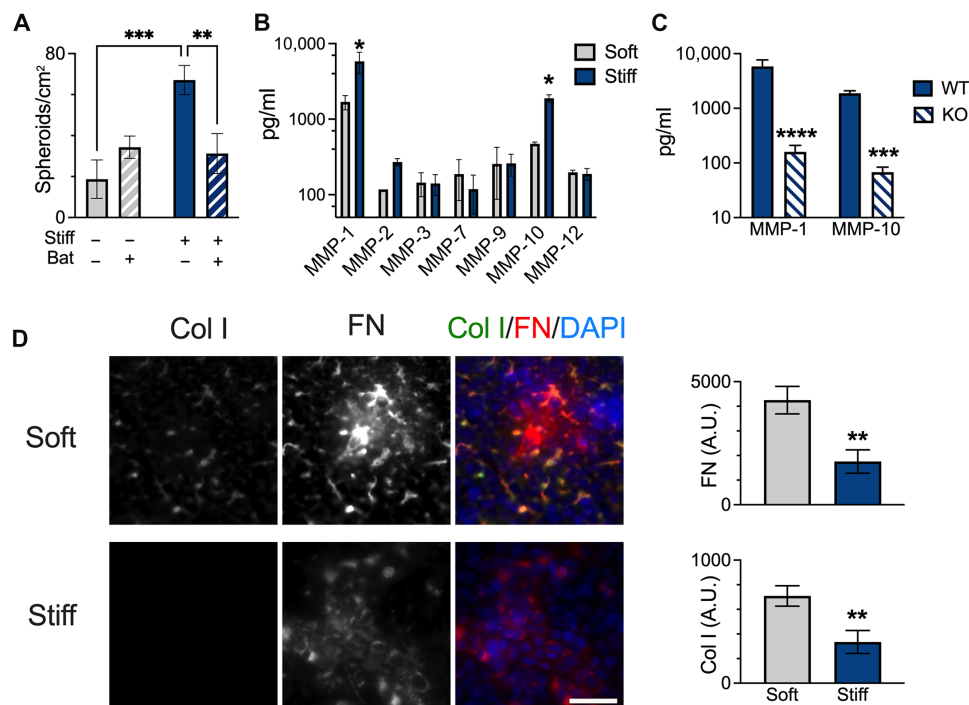
Fig. 4. Stiffness increases MMPs, leading to decreased ECM. (**A**) Quantification of Sph-CD from OV90 cells on soft or stiff gels treated with vehicle (DMSO) or 10 μM batimastat. (**B**) MMP concentrations for OV90 cells on soft or stiff gels. (**C**) MMP-1 and MMP-10 concentrations for WT OV90 [same data in (B)] or OV90 with *PIEZO1* knocked out by CRISPR on stiff gels. (**D**) Representative images and quantification of immunofluorescent staining of OV90 cells seeded on soft or stiff gels for 72 hours stained with CNA35-EGFP (to visualize deposited Col I) or antifibronectin. For (A) to (D), data shown are the average ± SD of N = 3 to 5 individual gels per condition. Statistical tests are two-way ANOVA with Tukey's (A), Sidak's multiple comparisons [(B) and (C)], and unpaired *t* test (D). *$P < 0.05$, **$P < 0.01$, ***$P < 0.001$, and ****$P < 0.0001$. Scale bars, 50 μm. FN, fibronectin.

HGSOC (Fig. 5A) (*37*). As OV90 cells showed the most robust response to stiffness and Piezo1, we tested OV90 and OV90-*PIEZO1*$^{-/-}$ cells. While prior reports stated that ascites does not develop with OV90 in nude mice (*38*), we observed a small volume of ascites by day 13 that was measurable at day 35 in *Scid* mice (Fig. 5B). Ascites volume was significantly larger in mice injected with wild-type OV90 compared to OV90-*PIEZO1*$^{-/-}$ cells. Nearly all mice had macroscopic tumors in the omentum by day 13, and all mice had macroscopic tumors in the omentum at day 35, regardless of Piezo1 status (Fig. 5C). Omental tumors increased in volume with time and did not show a difference in size with respect to Piezo1 expression (Fig. 5D). Similarly, nearly all mice injected with wild-type OV90 had visible tumors in the mesentery by day 13, and this increased to all mice at day 35. In contrast to the omentum, significantly fewer mice injected with OV90-*PIEZO1*$^{-/-}$ cells had macroscopic tumors in the mesentery at both time points (Fig. 5C). Tumors on the mesentery were substantially smaller than omental masses; because of the limited number of tumors in the OV90-*PIEZO1*$^{-/-}$ mice, it was not possible to compare tumor sizes, but a trend of smaller tumors with OV90-*PIEZO1*$^{-/-}$ was observed (Fig. 5D). A preference of ovarian cancer cells to colonize the omentum has been described in patients (*39*), and large tumors are present on the omentum after only a few weeks in the mouse model (*6*). Therefore, we hypothesized that the decrease in tumors in the mesentery resulted from a reduction of tumor spheroids released from the omental mass due to loss of Piezo1. Consistent with this hypothesis, we observed significantly fewer spheroids in ascites from mice injected with OV90-*PIEZO1*$^{-/-}$ cells (Fig. 5B; the spheroids

were similar in size; fig. S8A). Histological analysis of the mesentery at day 13 showed microscopic tumors on the mesentery in both mice (fig. S8B), and the percentage of tissue covered by tumor cells was lower but not significantly different (Fig. 5E). Overall, the data support that loss of Piezo1 has no impact on tumor initiation but may slow metastasis to the mesentery through a reduction in spheroid-based spread through the ascites.

DISCUSSION
Using an in vitro culture system to study the role of the microenvironment on collective detachment of HGSOC cells, we determined that increased stiffness resulted in an increased number of ovarian cancer spheroids. Single-cell detachment was unaffected, suggesting that the response to stiffness affected a step in the collective detachment process. Mechanistic investigations revealed that increased stiffness led to Piezo1 activation, which led to increased MMP levels and remodeling of Col I and fibronectin that promoted detachment. Interrupting this cascade by knockout of Piezo1 slowed progression in an in vivo model of HGSOC metastasis, with less ascites accumulation and lower tumor burden on the mesentery.

While the process of collective detachment has been proposed as a mechanism of HGSOC metastasis (*12*), there are many open questions surrounding how the process occurs and what factors regulate the release of single cells versus spheroids. We previously developed an in vitro model using a filter to separate Sph-CD from single cells and any spheroids that form by aggregation (Sph-SC). However, the
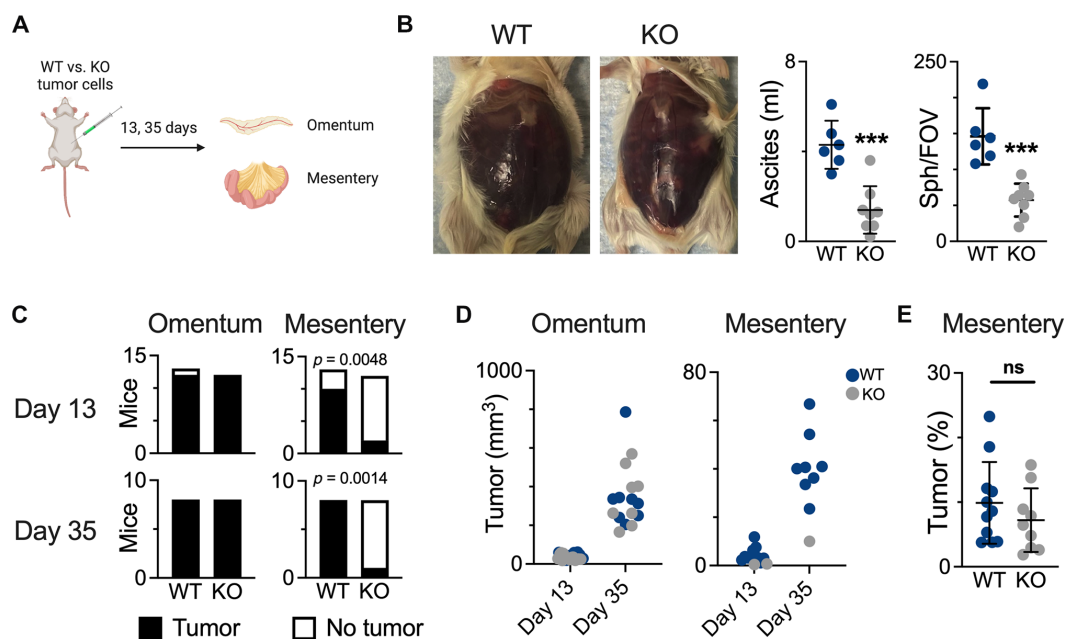
Fig. 5. Loss of *PIEZO1* slows metastasis to the mesentery. (**A**) Tumors were initiated by intraperitoneal injection of WT and *PIEZO*$^{-/-}$ OV90 cells. After 13 or 35 days, the omentum and mesentery were examined for tumor burden. (**B**) By 35 days, all mice developed ascites, with the volume significantly less in mice injected with OV90 with *PIEZO1* knocked out by CRISPR. Quantification of spheroids isolated from ascites fluid, data shown are average spheroids per field of view (FOV). $N = 6$ to 8 mice per group, with at least three fields of view averaged per mouse. ***$P < 0.001$ by unpaired t test. (**C**) Mice were categorized by the presence or absence of macroscopic tumors. $N = 12$ to 13 mice per group per time point. P values are for Fisher's exact test. (**D**) The total volume of all macroscopic tumors on the two tissue sites. Because of the low number of macroscopic tumors in the mesentery, statistics were not possible. (**E**) Hematoxylin and eosin (H&E)–stained sections of mesentery were imaged, and the percentage of tissue that was tumor was quantified. $N = 9$ to 11 mice per group, not significant by Mann-Whitney test. Data from day 13 were collected from a single trial. The day 35 data are a concatenation of two separate experiments; ascites collection was only conducted on the second trial.

physical setup of the model with a solid substrate under the cells means that it is possible that some Sph-CD form from single cells that quickly aggregated in solution before reaching the filter (*9*). Our results here support that most of the spheroids captured in the top filter are produced by collective detachment. First, if the Sph-CD arise from single cells that aggregate quickly, then we would expect to see a concomitant increase in single cells when Sph-CD increase; however, stiffness only affected Sph-CD numbers. Second, we observed bud-like structures on the monolayers that could be the source of Sph-CD. We note that Sph-CD were smaller in size than these buds (fig. S1G), consistent with our stiffness-dependent mechanism where MMP cleavage of ECM could release a group of cells. Elucidating the full mechanism of this process is beyond the scope of the current work but will likely identify additional approaches to limit collective detachment in metastasis. In addition, while we have focused to date on a monoculture to model the tumor, macrophages and fibroblasts are present in the surrounding tumor microenvironment. Their presence may be particularly important for ECM-based mechanisms as stromal fibroblasts are important to develop a robust fibronectin network (*40*) and ECM receptors such as DDR2 play roles in the stromal compartment in HGSOC (*41*).

Here, we sought to expand our model to test the hypothesis that changes in the tumor microenvironment associated with disease progression will increase collective detachment. While there are many changes in the microenvironment as tumors progress, it is well established that in HGSOC, the metastatic sites have increased Col I deposition and are substantially stiffer (*14, 18*). Separating the effects of increased Col I and stiffness is a nontrivial problem in many in vivo

and in vitro models; a further challenge is that most biomaterial approaches that do so cannot recreate the range of stiffnesses observed in metastatic HGSOC. Therefore, we used PAA gels, where the elastic modulus of the substrate can be varied independently of the density of adhesive ligands conjugated to the surface (*42, 43*). While this system cannot approximate a three-dimensional environment, it is an appropriate mimic for collective detachment in HGSOC as tumors are located along the tissue/peritoneal fluid boundary. While most studies use the PAA system to vary stiffness at a set ECM density, those examining combinations of stiffness and density have demonstrated effects by both on adhesion (*43*) and cell spreading (*44*). Similarly, in a three-dimensional model that can modulate Col I fiber density and bulk stiffness independently, both variables were found to affect breast cancer cell invasion (*45*). However, our results demonstrate an impact of stiffness that is independent of Col I density (Fig. 1), and others have shown that breast cancer cell response to prolactin stimulation was affected by stiffness alone (*46*). This reinforces that the influence of stiffness and ECM density should be considered both alone and in combination. Of course, the ECM of tumors includes components beyond Col I (*14*), so additional studies are needed to determine whether changes in ECM composition associated with HGSOC progression complement or counteract the impact of increased stiffness observed here.

To identify the mechanism responsible for the stiffness-induced increase in collective detachment, we considered the potential roles of proliferation (*47*), YAP (*48*), and Piezo1 (*49*). Consistent with our observation that Sph-CD may result from the bud-like structures on the cell monolayer, proliferation was necessary for robust bud formation

and increased Sph-CD but was not affected by the increase in stiffness. Likewise, YAP/TAZ was activated by stiffness but not responsible for the observed increase in Sph-CD (Fig. 2). Piezo1 is a stretch-activated ion channel that converts mechanical forces into cellular signaling through an influx of Ca^{2+} (49). Similar to others (50), we found Piezo1 expressed in HGSOC tumors but did not observe changes in Piezo1 expression in response to stiffness (Fig. 3). Piezo1 is activated by changes in membrane tension that open and close the ion channel, including shear stress (24) and substrate stiffness (51, 52). Through chemical inhibition, activation, and CRISPR knockout, we confirmed that Piezo1 activity is necessary for the stiffness-dependent increase in Sph-CD (Fig. 3). Cellular tractions were increased on stiffer substrates, and inhibiting actomyosin contractility decreased Sph-CD release, providing a potential mechanism by which substrate stiffness increases Piezo1 activity (31). Relevant to our context, Piezo1 was shown to regulate homeostatic non-apoptotic cell extrusion in epithelial monolayers, and inhibition of Piezo1 led to reduction of cell extrusion (26). However, we did not observe an increase in single-cell detachment with stiffness, suggesting that the findings here represent additional pathways by which Piezo1 can regulate epithelial cell organization. Piezo1 has been linked to other collective processes such as reepithelialization during wound healing, with loss of *Piezo1* accelerating wound healing in mice (53).

Given the data suggesting that Sph-CD detach from buds, we considered the potential for alterations in the ECM within the bud or monolayer. Stiffness did not affect expression of *COL1A1* or *FN1*, two of the most abundant ECM proteins in metastatic HGSOC (14). We observed changes in MMP-1 and/or MMP-10 in a subset of conditions, as well as decreases in Col I and fibronectin for all cell lines on stiffer substrates. This finding may seem in conflict with our prior study demonstrating a role for fibronectin in Sph-CD for reattachment; however, in that study, we demonstrated that the ECM was primarily produced by cells after they detached rather than taken from the substrate (9). Consistent with the proposed MMP-based mechanism, Piezo1 is linked to increased MMP-2 in endothelial cells (54) and human trabecular meshwork cells (55).

The finding of a MMP-based mechanism raises the question of whether the increase in MMPs on stiff matrices would be sufficient to soften the tumor microenvironment and perhaps enough to lessen spheroid production. The model system used in this work is a PAA gel; therefore, its stiffness was not susceptible to MMP degradation and softening. It was recently shown that a compressed collagen gel (elastic modulus, 4 kPa) treated with recombinant MMP-1 (800 ng/ml) softened from 4 to 1 kPa over 5 hours (56). While this would suggest we could see substantial softening, we note that the highest concentration of MMP-1 observed in our cultures was on the order of 10 ng/ml (80-fold less), which suggests that this effect would be slower or lessened—particularly as the stiffness in metastatic HGSOC is an order of magnitude higher. Correlating in vitro concentrations to in vivo settings is challenging, but we would expect that dilution in the ascites would result in lower concentrations. Our prior analysis of 14 patients undergoing primary debulking surgery found a maximum concentration MMP-1 (5 ng/ml) in ascites (57). It is possible that this question could be assessed using a polyethylene glycol–based system with MMP-degradable linkers (58); however, this will likely overestimate any softening relative to the in vivo setting, where surrounding fibroblasts would be depositing matrix at the same time as MMPs are active. Therefore, while we acknowledge that there may be local softening that could turn down the release of spheroids, we predict that the tumor bulk would remain at a pathophysiological stiffness.

On the basis of our in vitro findings, we next asked how loss of *PIEZO1* would affect tumor progression in vivo. A recent study found that *PIEZO1* knockdown in A1847 ovarian cancer cells slowed tumor growth and metastasis; however, this study used a subcutaneous xenograft (50) rather than an intraperitoneal xenograft that better mimics the patient's tumor microenvironment (37). We focused our analysis on the visceral fat deposits commonly involved in advanced HGSOC—the omentum (~80% of patients with stage III/IV HGSOC) and the mesentery (~30% of patients with stage III/IV HGSOC) (59). The high prevalence of tumors on the omentum suggests that it is an early site of distal metastasis. Our results demonstrated no effect of *PIEZO1* loss on tumor initiation or omental burden. As HGSOC progresses, tumor burden increases throughout the peritoneum, and there is an onset of ascites accumulation with larger volumes correlating to poor patient outcomes (60). With *PIEZO1* knocked out, we observed decreases in ascites fluid, number of tumor spheroids in this fluid, and macroscopic tumor numbers on the mesentery consistent with a reduction in overall metastatic burden.

These results are intriguing when we consider the differences between the untreated animal model and standard of care for patients. First, the finding of large omental disease is consistent with patient observations, where omental masses are dealt with by omentectomy during debulking surgery. The decrease in metastases on the mesentery suggests that *PIEZO1* inhibition could be used to reduce reseeding of the visceral adipose after debulking; this is particularly important as disease on the mesentery is often not amenable to surgical removal (61) and the challenges associated with recovery usually prohibit a second debulking surgery (62). In addition, the decrease in spheroids suggests that *PIEZO1* inhibition could be used to improve response to adjuvant chemotherapy as spheroids are more resistant to anoikis and chemotherapy (11). Future studies incorporating animal models of standard of care (63) could further clarify the impact of inhibiting *PIEZO1* on metastatic ovarian cancer and determine whether it is a promising target for therapy. Given the pleiotropic effects of Piezo1 throughout the body, this would likely be best done in combination with targeted delivery approaches (64).

MATERIALS AND METHODS
Unless noted, all materials were purchased from Thermo Fisher Scientific.

Cell lines
All experiments used ovarian cancer tumor cell lines OV90, OVCAR3, and OVCAR8 (American Type Culture Collection). Cell lines were authenticated by human short tandem repeat analysis at the TRIP Lab at the University of Wisconsin (UW)–Madison. Cells were cultured in 1:1 medium 199 (with Earle's salts and L-glutamine; Sigma-Aldrich, St. Louis, MO) and MCDB 105 medium (Sigma-Aldrich). Experiments were conducted in serum-free medium, and maintenance culture included 15% heat-inactivated fetal bovine serum. All media included 1% penicillin-streptomycin.

PAA gel preparation
The stiffness of a benign omentum (soft) and an omentum with metastatic disease (stiff) were estimated by a blinded gynecologic oncologist who manually palpated PAA gels over a range of stiffnesses

(Young's modulus from 2 to 44 kPa, values determined from stress-strain curve by dynamic mechanical analyzer, TA Instruments RA III). The "benign" tissue corresponded to 5 kPa (soft; 10% acrylamide and 0.03% bis-acrylamide), and the "metastatic" tissue corresponded to 44 kPa (stiff; 10% acrylamide and 0.45% bis-acrylamide; fig. S1A). For both gel conditions, 0.5% Irgacure-2959 was added as a photoinitiator (Advanced Biomatrix, Carlsbad, CA). Silanized glass coverslips (9 mm by 9 mm; Electron Microscopy Sciences, Hatfield, PA) were placed on top 19-µl drops of prepolymer solution and cross-linked under ultraviolet (UV) light at 254 nm for 15 min, producing gels with an approximate thickness of 235 µm (enough to ensure that cells cannot sense the coverslip stiffness) (65). Phosphate-buffered saline (PBS) was added, and the gels were swelled overnight. Sulfo-SANPAH (0.5 mg/ml) dissolved in 50 mM Hepes (pH 8.0) was added to gels, and UV light was applied for 25 min. Gels were washed twice in 50 mM Hepes and 2× in PBS on a shaker. A low (100 µg/ml) or high (2000 µg/ml) concentration of PureCol Collagen I (Advanced Biomatrix) diluted in PBS was added to the gels and incubated overnight [for experiments in Figs. 2 to 4, Col I (100 µg/ml) was used]. The Col I solution was aspirated, and 50 mM tris-HCl was added to the gels and incubated at room temperature for 15 min to quench any remaining sulfo-SANPAH. Gels were washed three times with PBS, and UV light was applied for 30 min to sterilize. Conjugation was confirmed by immunostaining with Col I primary antibody (1:500; Abcam, Waltham, MA; ab34710) and Alexa Fluor 488 goat anti-rabbit (1:500).

In vitro model

The in vitro model used in these experiments was described previously (9). Briefly, HGSOC cell lines (OV90, OVCAR3, or OVCAR8) were seeded onto PAA gels functionalized with Col I at a density of 926,000 cells/cm^2 in media with 15% serum for 4 hours. These gels were placed into a 40-µm cell strainer (Sigma-Aldrich) fitted into a six-well plate filled with 10 ml of serum-free media. After 72 hours, the Sph-CD were collected by removing the PAA gel from the filter, inverting the filter on top of a 50-ml conical tube and washing with 4 ml of serum-free media. Sph-SC were collected by filtering the medium from the culture plate through a separate 40-µm cell strainer and collecting the spheroids in the same manner as the Sph-CD spheroids. Single cells that had detached but not aggregated were collected from the media that had passed through the strainers. To quantify the number of Sph-CD, Sph-SC, or single cells that detached from each gel, the media was distributed in 0.5 ml of aliquots in a 48-well plate. Wells were imaged and analyzed in FIJI using a macro script (66). Briefly, background was subtracted, images were converted to binary, and "Fill Holes" used to fill holes were created by binary conversion. "Analyze Particles" was used to measure the area of objects and count them as single cells or spheroids. Particles were considered a spheroid if more than three cells could be visually identified and the diameter was greater than 20 µm; single cells had a 10- to 20-µm diameter. Spheroid buds were identified and counted manually; buds had a higher cell density and at least three cells with a raised z-position adjacent to one another (fig. S1).

Click-iT EdU

To visualize proliferating cells in the monolayer/buds, Click-iT 5-ethynyl 2′-deoxyuridine (EdU) Alexa Fluor 488 imaging was performed according to the manufacturer's instructions. OV90 cells were seeded on soft and stiff PAA gels and, after 42 hours of culture, changed to serum-free media supplemented with 10 µM EdU or dimethyl sulfoxide (DMSO) as a negative control. Six hours later (48 hours in total), cells were fixed, permeabilized, subjected to the Click-iT reaction, and imaged. Proliferating cells in the bulk of the monolayer and within buds were counted in FIJI, and the percentage of proliferating cells in the bulk and within buds was calculated.

Interventions

Aphidicolin (4 µg/ml), vertoporfin (2 µM), GsMTx-4 (10 µM), Yoda1 (10 µM), ML-7 (0.5 µM), or batimastat (10 µM) was incorporated into the media (Tocris, Bristol, United Kingdom) after cells had attached. An equivalent volume of DMSO was incorporated to account for vehicle effects. Fresh inhibitor/activator/vehicle was spiked into the medium every 24 hours.

Immunostaining

Cells were fixed in 4% paraformaldehyde for 15 to 25 min and blocked for 45 to 60 min in 10% goat serum or 10% donkey serum. Piezo1 primary antibody (1:200; Proteintech, San Diego, CA) and YAP primary antibody (1:500; Cell Signaling Technologies, Danvers, MA) were applied overnight at 4°C. Secondary antibody [Alexa Fluor 488 goat anti-rabbit (1:500) or Alexa Fluor 647 donkey anti-rabbit (1:250)] was applied for 1 hour at room temperature. Cells were counter-stained with Hoechst 33258 (1:500) for 5 min at room temperature. To visualize deposited Col I and fibronectin, paraformaldehyde-fixed samples were incubated with 50 µM CNA35-EGFP (36) in 5% bovine serum albumin (BSA) at 37°C overnight. After washing (0.1% BSA in PBS) at least 3 times for 30 min each, fibronectin primary antibody in 5% BSA (1:100; Abcam, ab2413) was applied overnight at 4°C. Secondary antibody (1:200; Alexa Fluor 647 goat anti-rabbit) was applied for 1 hour at room temperature, and cells were counterstained with Hoechst 33342 (1:500) for 15 min at room temperature.

Formalin-fixed, paraffin-embedded samples from patients who had undergone surgical debulking for HGSOC or other conditions were obtained from archived pathology samples through a protocol approved by the UW-Madison Institutional Review Board (IRB) (table S1). Sections (5 µm) were prepared by the TRIP lab (UW Carbone Cancer Center), deparaffinized, subjected to antigen retrieval, and blocked with 10% goat serum. Primary antibodies for Piezo1 (1:500; Novus Biologicals, Centennial, CO) and pan-cytokeratin (1:500; OriGene, Rockville, MD) were applied overnight at 4°C. Secondary antibodies [Alexa Fluor 488 goat anti-rabbit (1:500) and Alexa Fluor 647 goat anti-guinea pig (1:500)] were applied at room temperature for 1 hour. Slides were mounted using ProLong Diamond Antifade with 4′,6-diamidino-2-phenylindole.

For all staining, a no primary control was included to account for nonspecific signal. All imaging was done on a Zeiss Axio Observer.Z1 inverted microscope with an AxioCam 506 mono camera and a Plan-Apochromat 10× 0.4–numerical aperture (NA) or 20× 0.8-NA air objective. Coverslips with PAA gels were inverted on coverslips to improve focus while imaging. For quantification of staining, the mean fluorescent intensity was measured in FIJI, and the background was subtracted on the basis of measurement of controls without primary antibodies. For each individual gel, the mean value of at least three analyzed images is reported.

Quantitative reverse transcription polymerase chain reaction

RNA was isolated from cells on the monolayer of soft and stiff substrates at 72 hours using the Monarch Total RNA Miniprep Kit (New

England Biolabs, Ipswich, MA). The quality and amount of isolated RNA were determined using a NanoDrop One, and cDNA was synthesized by SuperScript III First-Strand Synthesis. Quantitect primers for *PIEZO1*, *COL1A1*, and *FN1* (Qiagen, Germantown, MD) were used in combination with SsoAdvanced Universal SYBR Green Supermix (Bio-Rad, Hercules, CA) on a CFX Connect Real-Time PCR Detection System (Bio-Rad).

Traction force microscopy
For traction force microscopy, PAA gels with a thickness of 100 μm were prepared using the formulations above with fluorescent particles (0.5 μm in diameter, red, Life Technologies). Glass coverslips (18 mm in diameter) were hydrophobically treated to prevent sticking to the gel by dipping each coverslip in a solution of 97% hexane, 0.5% acetic acid, and 2.5% (tridecafluoro-1,1,2,2-tetrahydrooctyl) triethoxysilane and air drying overnight. No. 1.5 glass-bottom dishes (Cellvis, Mountain View, CA) were treated as described previously (*67*), 20 μl of the gel solution was pipetted onto each dish, and a coverslip was placed on top. The dishes were placed upside-down in a centrifuge and spun for 3 min at 15 relative centrifugal force to localize the fluorescent particles to the top of each gel. Dishes were carefully removed, exposed to UV light at 254 nm for 15 min, and then swelled overnight in Dulbecco's Phosphate-Buffered Saline. Gels were conjugated with ECM and seeded as above; after 24 hours, images were collected of the cells (phase contrast) and particles (fluorescence) using the Zeiss microscope at 37°C. The cells were removed from the substrates by adding trypsin, which allowed the PAA substrates to recover to an undeformed reference state, and the fluorescent particles were imaged again. Fast Iterative Digital Image Correlation was used to measure cell-generated substrate displacements with respect to the undeformed reference images (*68*). Tractions were calculated using unconstrained Fourier transform traction cytometry (*69*) with a correction for finite substrate thickness (*70*, *71*). The results yielded the traction vector field applied by the cells to the substrate.

PIEZO1 CRISPR
CRISPR-Cas9 was used to knock out *PIEZO1* in OV90, OVCAR3, and OVCAR8. Three *PIEZO1* guide RNA (gRNA) sequence oligos (sequences 1 to 3; table S2) designed and validated from the Zhang lab at the Broad Institute were selected and synthesized (Integrated DNA Technologies, Coralville, IA) (*28*). lentiCRISPR v2 was a gift from F. Zhang (Addgene plasmid #52961; http://n2t.net/addgene:52961; RRID:Addgene_52961); this one vector system delivers hSpCas9 and chimeric gRNA expression cassettes (*28*). The lentiCRISPRv2 vector was dephosphorylated and digested with Bsm BI restriction enzyme and subsequently gel-purified. The forward and reverse gRNA oligos were phosphorylated, annealed, and ligated into the cut vector. Whole plasmid sequencing (Plasmidsaurus, Eugene, OR) was used to confirm *PIEZO1* gRNA insertion into the lentiCRISPRv2 construct.

One Shot Stbl3 chemically competent *Escherichia coli* were transformed with the *PIEZO1* lentiCRISPRv2 plasmid and grown in LB with ampicillin (100 μg/ml) for selection and expansion. Human embryonic kidney 293T cells were cotransfected with packaging plasmids from the Lenti-vpak Lentiviral Packaging Kit (Origene) and the *PIEZO1* lentiCRISPRv2 plasmid. After 48 and 72 hours of incubation, viral batches were collected and combined for each gene target; an equal volume of virus constructs with *PIEZO1* gRNA 1, 2, and 3 were used to increase the probability of an effective gene edit. The viral supernatant was added to each cell line at a 2:3 virus to ovarian cancer media volume ratio. Polybrene was added at 8 μg/ml, and the plate was centrifuged at 165*g* for 2 hours to aid transduction. After incubation for 48 hours, puromycin (4 μg/ml) was added for an additional 48 hours for selection. Knockout was verified by qRT-PCR for *PIEZO1* (Qiagen, Hilden, Germany) and immunostaining.

MMP quantification
Media was collected 72 hours after seeding from cells on soft and stiff gels, soft gels were treated with Yoda1, and stiff gels were seeded with *PIEZO1* knockout cells. Media was centrifuged, and the supernatant was snap-frozen in liquid nitrogen and quantified by Eve Technologies (Calgary, Canada) using a bead-based multiplex immunoassay for MMP-1, MMP-2, MMP-3, MMP-7, MMP-8, MMP-9, MMP-10, MMP-12, and MMP-13. MMP-1 readings from some samples were near the saturation limit; therefore, all samples were assayed at up to a 1:50 dilution using an MMP-1–specific enzyme-linked immunosorbent assay (Abcam).

In vivo studies
Female BALB/c *scid* (CBySmn.Cg-*Prkdc*^{scid}/J) mice (approximately 10 weeks of age) were procured from the Jackson Laboratory (Bar Harbor, ME). All animal protocols were approved by the Institutional Animal Care and Use Committee (IACUC) at the UW-Madison School of Medicine and Public Health. Mice were intraperitoneally injected with 2 million OV90 or OV90-*PIEZO1*$^{-/-}$ cells in 100 μl and euthanized by CO_2 asphyxiation after 13 or 35 days. Ascites was removed from the mice at day 35 using 22 ½ gauge needle, and the approximate volumes of ascites were recorded. The peritoneal cavity was then washed by injection of 4 ml of PBS, and the collected ascites/PBS was filtered through a 40-μm filter to isolate spheroids for quantification as above (Fig. 1A). Mice were necropsied, and macroscopic tumor numbers on the omentum and mesentery were counted and measured by a digital caliper. The volume (*V*) of the macroscopic tumors was approximated using the formula $V = 1/2 \times$ tumor width (*W*) × tumor width (*W*) × tumor length (L) (*72*). Tissue samples were fixed, paraffin-embedded, sectioned, and stained with hematoxylin and eosin (H&E). Images of the whole H&E-stained tissue sections were acquired with a Zeiss Axio Observer.Z1 inverted microscope using the Tiles tool. Microscopic tumor lesions were outlined on the images and analyzed by ImageJ. Microscopic tumor burden was defined as the area of a tissue section occupied by tumors divided by the total area of the tissue section.

Statistics
Statistical tests are detailed in figure legends and were performed in GraphPad Prism, and $P < 0.05$ was considered significant. All in vitro experiments were performed at least twice with one representative experiment shown.

Research standards
Animal protocols were approved by the IACUC at the UW-Madison School of Medicine and Public Health. Tissue samples from human patients were obtained with a consent waiver due to de-identification procedures approved by the UW-Madison IRB.

Supplementary Materials

This PDF file includes:
Figs. S1 to S8
Tables S1 and S2

REFERENCES AND NOTES

1. A. S. O'Shea, Clinical staging of ovarian cancer. *Methods Mol. Biol.* **2424**, 3–10 (2022).
2. H. M. Micek, M. R. Visetsouk, A. J. Fleszar, P. K. Kreeger, The many microenvironments of ovarian cancer. *Adv. Exp. Med. Biol.* **1296**, 199–213 (2020).
3. H. A. Kenny, C. Y. Chiang, E. A. White, E. M. Schryver, M. Habis, I. L. Romero, A. Ladanyi, C. V. Penicka, J. George, K. Matlin, A. Montag, K. Wroblewski, S. D. Yamada, A. P. Mazar, D. Bowtell, E. Lengyel, Mesothelial cells promote early ovarian cancer metastasis through fibronectin secretion. *J. Clin. Invest.* **124**, 4614–4628 (2014).
4. C. M. Novak, E. N. Horst, E. Lin, G. Mehta, Compressive stimulation enhances ovarian cancer proliferation, invasion, chemoresistance, and mechanotransduction via CDC42 in a 3D bioreactor. *Cancers* **12**, 1521 (2020).
5. A. Russo, Z. Yang, G. M. Heyrman, B. P. Cain, A. Lopez Carrero, B. C. Isenberg, M. J. Dean, J. Coppeta, J. E. Burdette, Versican secreted by the ovary links ovulation and migration in fallopian tube derived serous cancer. *Cancer Lett.* **543**, 215779 (2022).
6. E. I. Harper, T. S. Hilliard, In Vivo and ex vivo analysis of omental adhesion in ovarian cancer. *Methods Mol. Biol.* **2424**, 199–216 (2022).
7. S. Mittal, P. Gupta, P. Chaluvally-Raghavan, S. Pradeep, Establishment of In Vivo ovarian cancer mouse models using intraperitoneal tumor cell injection. *Methods Mol. Biol.* **2424**, 247–254 (2022).
8. M. Asem, A. Young, C. Oyama, A. ClaureDeLaZerda, Y. Liu, M. J. Ravosa, V. Gupta, A. Jewell, D. Khabele, M. S. Stack, Ascites-induced compression alters the peritoneal microenvironment and promotes metastatic success in ovarian cancer. *Sci. Rep.* **10**, 11913 (2020).
9. H. M. Micek, L. Rosenstock, Y. Ma, C. Hielsberg, L. Montemorano, M. K. Gari, S. M. Ponik, P. K. Kreeger, Model of collective detachment in high-grade serous ovarian cancer demonstrates that tumor spheroids produce ECM to support metastatic processes. *APL Bioeng.* **7**, 016111 (2023).
10. S. Miceska, E. Skof, G. Gasljevic, V. Kloboves-Prevodnik, Morphological and immunocytochemical characterization of tumor spheroids in ascites from high-grade serous carcinoma. *Cells* **12**, 2390 (2023).
11. S. Makhija, D. D. Taylor, R. K. Gibb, C. Gercel-Taylor, Taxol-induced bcl-2 phosphorylation in ovarian cancer cell monolayer and spheroids. *Int. J. Oncol.* **14**, 515–521 (1999).
12. S. Al Habyan, C. Kalos, J. Szymborski, L. McCaffrey, Multicellular detachment generates metastatic spheroids during intra-abdominal dissemination in epithelial ovarian cancer. *Oncogene* **37**, 5127–5135 (2018).
13. H. M. Micek, M. R. Visetsouk, K. S. Masters, P. K. Kreeger, Engineering the extracellular matrix to model the evolving tumor microenvironment. *iScience* **23**, 101742 (2020).
14. O. M. T. Pearce, R. M. Delaine-Smith, E. Maniati, S. Nichols, J. Wang, S. Bohm, V. Rajeeve, D. Ullah, P. Chakravarty, R. R. Jones, A. Montfort, T. Dowe, J. Gribben, J. L. Jones, H. M. Kocher, J. S. Serody, B. G. Vincent, J. Connelly, J. D. Brenton, C. Chelala, P. R. Cutillas, M. Lockley, C. Bessant, M. M. Knight, F. R. Balkwill, Deconstruction of a metastatic tumor microenvironment reveals a common matrix response in human cancers. *Cancer Discov.* **8**, 304–319 (2018).
15. K. J. Cheung, A. J. Ewald, A collective route to metastasis: Seeding by tumor cell clusters. *Science* **352**, 167–169 (2016).
16. N. Alkhouli, J. Mansfield, E. Green, J. Bell, B. Knight, N. Liversedge, J. C. Tham, R. Welbourn, A. C. Shore, K. Kos, C. P. Winlove, The mechanical properties of human adipose tissues and their relationships to the structure and composition of the extracellular matrix. *Am. J. Physiol. Endocrinol. Metab.* **305**, E1427–E1435 (2013).
17. R. M. Delaine-Smith, S. Burney, F. R. Balkwill, M. M. Knight, Experimental validation of a flat punch indentation methodology calibrated against unconfined compression tests for determination of soft tissue biomechanics. *J. Mech. Behav. Biomed. Mater.* **60**, 401–415 (2016).
18. K. C. Fogg, C. M. Renner, H. Christian, A. Walker, L. Marty-Santos, A. Khan, W. R. Olson, C. Parent, A. O'Shea, D. M. Wellik, P. S. Weisman, P. K. Kreeger, Ovarian cells have increased proliferation in response to heparin-binding epidermal growth factor as collagen density increases. *Tissue Eng. Part A* **26**, 747–758 (2020).
19. J. J. Northey, A. S. Barrett, I. Acerbi, M. K. Hayward, S. Talamantes, I. S. Dean, J. K. Mouw, S. M. Ponik, J. N. Lakins, P. J. Huang, J. Wu, Q. Shi, S. Samson, P. J. Keely, R. A. Mukhtar, J. T. Liphardt, J. A. Shepherd, E. S. Hwang, Y. Y. Chen, K. C. Hansen, L. E. Littlepage, V. M. Weaver, Stiff stroma increases breast cancer risk by inducing the oncogene ZNF217. *J. Clin. Invest.* **130**, 5721–5737 (2020).
20. T. A. Ulrich, E. M. de Juan Pardo, S. Kumar, The mechanical rigidity of the extracellular matrix regulates the structure, motility, and proliferation of glioma cells. *Cancer Res.* **69**, 4167–4174 (2009).
21. M. Jang, J. An, S. W. Oh, J. Y. Lim, J. Kim, J. K. Choi, J. H. Cheong, P. Kim, Matrix stiffness epigenetically regulates the oncogenic activation of the Yes-associated protein in gastric cancer. *Nat. Biomed. Eng.* **5**, 114–123 (2021).
22. S. W. Chan, C. J. Lim, K. Guo, C. P. Ng, I. Lee, W. Hunziker, Q. Zeng, W. Hong, A role for TAZ in migration, invasion, and tumorigenesis of breast cancer cells. *Cancer Res.* **68**, 2592–2598 (2008).
23. C. Wang, X. Zhu, W. Feng, Y. Yu, K. Jeong, W. Guo, Y. Lu, G. B. Mills, Verteporfin inhibits YAP function through up-regulating 14-3-3σ sequestering YAP in the cytoplasm. *Am. J. Cancer Res.* **6**, 27–37 (2016).
24. S. S. Ranade, Z. Qiu, S. H. Woo, S. S. Hur, S. E. Murthy, S. M. Cahalan, J. Xu, J. Mathur, M. Bandell, B. Coste, Y. S. Li, S. Chien, A. Patapoutian, Piezo1, a mechanically activated ion channel, is required for vascular development in mice. *Proc. Natl. Acad. Sci. U.S.A.* **111**, 10347–10352 (2014).
25. K. Diem, M. Fauler, G. Fois, A. Hellmann, N. Winokurow, S. Schumacher, C. Kranz, M. Frick, Mechanical stretch activates piezo1 in caveolae of alveolar type I cells to trigger ATP release and paracrine stimulation of surfactant secretion from alveolar type II cells. *FASEB J.* **34**, 12785–12804 (2020).
26. G. T. Eisenhoffer, P. D. Loftus, M. Yoshigi, H. Otsuna, C. B. Chien, P. A. Morcos, J. Rosenblatt, Crowding induces live cell extrusion to maintain homeostatic cell numbers in epithelia. *Nature* **484**, 546–549 (2012).
27. C. Bae, F. Sachs, P. A. Gottlieb, The mechanosensitive ion channel Piezo1 is inhibited by the peptide GsMTx4. *Biochemistry* **50**, 6295–6300 (2011).
28. N. E. Sanjana, O. Shalem, F. Zhang, Improved vectors and genome-wide libraries for CRISPR screening. *Nat. Methods* **11**, 783–784 (2014).
29. W. M. Botello-Smith, W. Jiang, H. Zhang, A. D. Ozkan, Y. C. Lin, C. N. Pham, J. J. Lacroix, Y. Luo, A mechanism for the activation of the mechanosensitive Piezo1 channel by the small molecule Yoda1. *Nat. Commun.* **10**, 4503 (2019).
30. A. H. Lewis, J. Grandl, Mechanical sensitivity of Piezo1 ion channels can be tuned by cellular membrane tension. *eLife* **4**, (2015).
31. K. L. Ellefsen, J. R. Holt, A. C. Chang, J. L. Nourse, J. Arulmoli, A. H. Mekhdjian, H. Abuwarda, F. Tombola, L. A. Flanagan, A. R. Dunn, I. Parker, M. M. Pathak, Myosin-II mediated traction forces evoke localized Piezo1-dependent Ca(2+) flickers. *Commun. Biol.* **2**, 298 (2019).
32. W. Morozumi, K. Aoshima, S. Inagaki, Y. Iwata, S. Nakamura, H. Hara, M. Shimazawa, Piezo 1 is involved in intraocular pressure regulation. *J. Pharmacol. Sci.* **147**, 211–221 (2021).
33. Y. Yu, X. Wu, S. Liu, H. Zhao, B. Li, H. Zhao, X. Feng, Piezo1 regulates migration and invasion of breast cancer cells via modulating cell mechanobiological properties. *Acta Biochim. Biophys. Sin. (Shanghai)* **53**, 10–18 (2021).
34. P. A. Arakaki, M. R. Marques, M. C. Santos, MMP-1 polymorphism and its relationship to pathological processes. *J. Biosci.* **34**, 313–320 (2009).
35. S. Bord, A. Horner, R. M. Hembry, J. E. Compston, Stromelysin-1 (MMP-3) and stromelysin-2 (MMP-10) expression in developing human bone: Potential roles in skeletal development. *Bone* **23**, 7–12 (1998).
36. S. J. Aper, A. C. van Spreeuwel, M. C. van Turnhout, A. J. van der Linden, P. A. Pieters, N. L. van der Zon, S. L. de la Rambelje, C. V. Bouten, M. Merkx, Colorful protein-based fluorescent probes for collagen imaging. *PLOS ONE* **9**, e114983 (2014).
37. A. K. Mitra, D. A. Davis, S. Tomar, L. Roy, H. Gurler, J. Xie, D. D. Lantvit, H. Cardenas, F. Fang, Y. Liu, E. Loughran, J. Yang, M. Sharon Stack, R. E. Emerson, K. D. Cowden Dahl, M. V. Barbolina, K. P. Nephew, D. Matei, J. E. Burdette, In vivo tumor growth of high-grade serous ovarian cancer cell lines. *Gynecol. Oncol.* **138**, 372–377 (2015).
38. L. Hernandez, M. K. Kim, L. T. Lyle, K. P. Bunch, C. D. House, F. Ning, A. M. Noonan, C. M. Annunziata, Characterization of ovarian cancer cell lines as in vivo models for preclinical studies. *Gynecol. Oncol.* **142**, 332–340 (2016).
39. K. M. Nieman, H. A. Kenny, C. V. Penicka, A. Ladanyi, R. Buell-Gutbrod, M. R. Zillhardt, I. L. Romero, M. S. Carey, G. B. Mills, G. S. Hotamisligil, S. D. Yamada, M. E. Peter, K. Gwin, E. Lengyel, Adipocytes promote ovarian cancer metastasis and provide energy for rapid tumor growth. *Nat. Med.* **17**, 1498–1503 (2011).
40. S. Libring, A. Shinde, M. K. Chanda, M. Nuru, H. George, A. M. Saleh, A. Abdullah, T. L. Kinzer-Ursem, S. Calve, M. K. Wendt, L. Solorio, The dynamic relationship of breast cancer cells and fibroblasts in fibronectin accumulation at primary and metastatic tumor sites. *Cancers (Basel)* **12**, 1270 (2020).
41. A. M. Schab, M. M. Greenwade, E. Stock, E. Lomonosova, K. Cho, W. R. Grither, H. Noia, D. Wilke, M. M. Mullen, A. R. Hagemann, I. S. Hagemann, P. H. Thaker, L. M. Kuroki, C. K. McCourt, D. Khabele, M. A. Powell, D. G. Mutch, P. Zhao, L. P. Shriver, G. J. Patti, G. D. Longmore, K. C. Fuh, Stromal DDR2 promotes ovarian cancer metastasis through regulation of metabolism and secretion of extracellular matrix proteins. *Mol. Cancer Res.* **21**, 1234–1248 (2023).
42. R. J. Pelham Jr., Y. Wang, Cell locomotion and focal adhesions are regulated by substrate flexibility. *Proc. Natl. Acad. Sci. U.S.A.* **94**, 13661–13665 (1997).
43. J. D. Mih, A. S. Sharif, F. Liu, A. Marinkovic, M. M. Symer, D. J. Tschumperlin, A multiwell platform for studying stiffness-dependent cell biology. *PLOS ONE* **6**, e19929 (2011).
44. A. Engler, L. Bacakova, C. Newman, A. Hategan, M. Griffin, D. Discher, Substrate compliance versus ligand density in cell on gel responses. *Biophys. J.* **86**, 617–628 (2004).

45. A. J. Berger, K. M. Linsmeier, P. K. Kreeger, K. S. Masters, Decoupling the effects of stiffness and fiber density on cellular behaviors via an interpenetrating network of gelatin-methacrylate and collagen. *Biomaterials* **141**, 125–135 (2017).

46. C. E. Barcus, P. J. Keely, K. W. Eliceiri, L. A. Schuler, Stiff collagen matrices increase tumorigenic prolactin signaling in breast cancer cells. *J. Biol. Chem.* **288**, 12722–12732 (2013).

47. J. Schrader, T. T. Gordon-Walker, R. L. Aucott, M. van Deemter, A. Quaas, S. Walsh, D. Benten, S. J. Forbes, R. G. Wells, J. P. Iredale, Matrix stiffness modulates proliferation, chemotherapeutic response, and dormancy in hepatocellular carcinoma cells. *Hepatology* **53**, 1192–1205 (2011).

48. S. Dupont, L. Morsut, M. Aragona, E. Enzo, S. Giulitti, M. Cordenonsi, F. Zanconato, J. Le Digabel, M. Forcato, S. Bicciato, N. Elvassore, S. Piccolo, Role of YAP/TAZ in mechanotransduction. *Nature* **474**, 179–183 (2011).

49. B. Coste, J. Mathur, M. Schmidt, T. J. Earley, S. Ranade, M. J. Petrus, A. E. Dubin, A. Patapoutian, Piezo1 and Piezo2 are essential components of distinct mechanically activated cation channels. *Science* **330**, 55–60 (2010).

50. Y. Xiong, L. Dong, Y. Bai, H. Tang, S. Li, D. Luo, F. Liu, J. Bai, S. Yang, X. Song, Piezo1 activation facilitates ovarian cancer metastasis via Hippo/YAP signaling axis. *Channels (Austin)* **16**, 159–166 (2022).

51. M. Lopez-Cavestany, S. B. Hahn, J. M. Hope, N. T. Reckhorn, J. D. Greenlee, S. C. Schwager, J. A. VanderBurgh, C. A. Reinhart-King, M. R. King, Matrix stiffness induces epithelial-to-mesenchymal transition via Piezo1-regulated calcium flux in prostate cancer cells. *iScience* **26**, 106275 (2023).

52. M. M. Pathak, J. L. Nourse, T. Tran, J. Hwe, J. Arulmoli, D. T. Le, E. Bernardis, L. A. Flanagan, F. Tombola, Stretch-activated ion channel Piezo1 directs lineage choice in human neural stem cells. *Proc. Natl. Acad. Sci. U.S.A.* **111**, 16148–16153 (2014).

53. J. R. Holt, W.-Z. Zeng, E. L. Evans, S.-H. Woo, S. Ma, H. Abuwarda, A. Patapoutian, M. M. Pathak, (BioRxiv, 2020).

54. H. Kang, Z. Hong, M. Zhong, J. Klomp, K. J. Bayless, D. Mehta, A. V. Karginov, G. Hu, A. B. Malik, Piezo1 mediates angiogenesis through activation of MT1-MMP signaling. *Am. J. Physiol. Cell Physiol.* **316**, C92–C103 (2019).

55. W. Morozumi, K. Aoshima, S. Inagaki, Y. Iwata, Y. Takagi, S. Nakamura, H. Hara, M. Shimazawa, Piezo1 activation induces fibronectin reduction and PGF2α secretion via arachidonic acid cascade. *Exp. Eye Res.* **215**, 108917 (2022).

56. A. Micalet, J. Pape, D. Bakkalci, Y. Javanmardi, C. Hall, U. Cheema, E. Moeendarbary, Evaluating the impact of a biomimetic mechanical environment on cancer invasion and matrix remodeling. *Adv. Healthc. Mater.* **12**, e2201749 (2023).

57. M. J. Carroll, K. Kaipio, J. Hynninen, O. Carpen, S. Hautaniemi, D. Page, P. K. Kreeger, A subset of secreted proteins in ascites can predict platinum-free interval in ovarian cancer. *Cancers (Basel)* **14**, 4291 (2022).

58. J. L. Leight, D. L. Alge, A. J. Maier, K. S. Anseth, Direct measurement of matrix metalloproteinase activity in 3D cellular microenvironments using a fluorogenic peptide substrate. *Biomaterials* **34**, 7344–7352 (2013).

59. J. Prat; FIGO Committee on Gynecologic Oncology, Staging classification for cancer of the ovary, fallopian tube, and peritoneum. *Int. J. Gynaecol. Obstet.* **124**, 1–5 (2014).

60. J. B. Szender, T. Emmons, S. Belliotti, D. Dickson, A. Khan, K. Morrell, A. Khan, K. L. Singel, P. C. Mayor, K. B. Moysich, K. Odunsi, B. H. Segal, K. H. Eng, Impact of ascites volume on clinical outcomes in ovarian cancer: A cohort study. *Gynecol. Oncol.* **146**, 491–497 (2017).

61. A. H. Brand, Ovarian cancer debulking surgery: A survey of practice in Australia and New Zealand. *Int. J. Gynecol. Cancer* **21**, 230–235 (2011).

62. M. Pergolotti, A. Bailliard, L. McCarthy, E. Farley, K. R. Covington, K. M. Doll, Women's experiences after ovarian cancer surgery: Distress, uncertainty, and the need for occupational therapy. *Am. J. Occup. Ther.* **74**, 7403205140p1–7403205140p9 (2020).

63. M. Popa, V. Fosse, K. Kleinmanns, L. Bjorge, E. McCormack, Xenograft models of ovarian cancer for therapy evaluation. *Methods Mol. Biol.* **2424**, 275–293 (2022).

64. S. Correa, N. Boehnke, A. E. Barberio, E. Deiss-Yehiely, A. Shi, B. Oberlton, S. G. Smith, I. Zervantonakis, E. C. Dreaden, P. T. Hammond, Tuning nanoparticle interactions with ovarian cancer through layer-by-layer modification of surface chemistry. *ACS Nano* **14**, 2224–2237 (2020).

65. S. Sen, A. J. Engler, D. E. Discher, Matrix strains induced by cells: Computing how far cells can feel. *Cell. Mol. Bioeng.* **2**, 39–48 (2009).

66. J. Schindelin, I. Arganda-Carreras, E. Frise, V. Kaynig, M. Longair, T. Pietzsch, S. Preibisch, C. Rueden, S. Saalfeld, B. Schmid, J. Y. Tinevez, D. J. White, V. Hartenstein, K. Eliceiri, P. Tomancak, A. Cardona, Fiji: An open-source platform for biological-image analysis. *Nat. Methods* **9**, 676–682 (2012).

67. K. Vazquez, A. Saraswathibhatla, J. Notbohm, Effect of substrate stiffness on friction in collective cell migration. *Sci. Rep.* **12**, 2474 (2022).

68. E. Bar-Kochba, J. Toyjanova, E. Andrews, K.-S. Kim, C. Franck, A fast iterative digital volume correlation algorithm for large deformations. *Exp. Mech.* **55**, 261–274 (2015).

69. J. P. Butler, I. M. Tolic-Norrelykke, B. Fabry, J. J. Fredberg, Traction fields, moments, and strain energy that cells exert on their surroundings. *Am. J. Physiol. Cell Physiol.* **282**, C595–C605 (2002).

70. X. Trepat, M. R. Wasserman, T. E. Angelini, E. Millet, D. A. Weitz, J. P. Butler, J. J. Fredberg, Physical forces during collective cell migration. *Nat. Phys.* **5**, 426–430 (2009).

71. J. C. del Alamo, R. Meili, B. Alonso-Latorre, J. Rodriguez-Rodriguez, A. Aliseda, R. A. Firtel, J. C. Lasheras, Spatio-temporal analysis of eukaryotic cell motility by improved force cytometry. *Proc. Natl. Acad. Sci. U.S.A.* **104**, 13343–13348 (2007).

72. A. Faustino-Rocha, P. A. Oliveira, J. Pinho-Oliveira, C. Teixeira-Guedes, R. Soares-Maia, R. G. da Costa, B. Colaco, M. J. Pires, J. Colaco, R. Ferreira, M. Ginja, Estimation of rat mammary tumor volume using caliper and ultrasonography measurements. *Lab. Anim. (NY)* **42**, 217–224 (2013).